A Portable K-Band 3-D MIMO Radar With Nonuniformly Spaced Array for Short-Range Localization

Zhengyu Peng, *Student Member, IEEE*, and Changzhi Li, *Senior Member, IEEE*

Abstract—This paper presents a K-band multiple-input-multiple-output (MIMO) radar for short-range localization. This radar features 3-D imaging capability, which can obtain the range, azimuth angle, and zenith angle of a target. The proposed radar system implements the concept of MIMO to synthesize a planar array that realizes 2-D digital beamforming with a small number of transmitter and receiver (T/R) channels. A nonuniformly spaced array configuration is also designed to further reduce the number of T/R channels without sacrificing the beamwidth and sidelobe level. The design principle is detailed in this paper. A prototype with eight transmitter channels and eight receiver channels has been built. A calibration procedure was developed to remove path delays of different MIMO channels. Experiments of the proposed K-band MIMO radar prototype reveal its capability in the 3-D localization of multiple targets. This prototype features 7.2° 2-D angular resolution, 90° field of view, −10-dB sidelobe level, and wireless data transfer.

Index Terms—Frequency-modulated continuous-wave (FMCW) radar, K-band, multiple-input-multiple-output (MIMO) radar, short-range localization, time-division multiplexing (TDM).

I. INTRODUCTION

IN RECENT years, applications of radar systems have been extended to many commercial areas, such as through-the-wall detections [1], [2], indoor localization [3], driver assistance [4], [5], and biomedical applications [6]–[8]. Phased array and digital beamforming techniques have enabled a radar system with electrical beam-scanning capability, which features lightweight, low profile, and high steering speed compared to mechanical steering systems [9], [10].

A conventional way to realize a phased array is using phase shifters to control the phase of each antenna element in an array [9]. This approach can be extended to an RF beamforming architecture. In an RF beamforming system, the dedicated phase shifter for each antenna element dramatically increases the hardware complexity and cost, especially when the frequency goes up to the millimeter-wave region for

5G and automotive radar applications. In addition, conventional phase shifters also suffer from phase errors and limitations on resolution and bandwidth [11], [12]. Researchers have introduced special typologies, such as true time-delay beam steering [13]–[15] and all-pass networks [16], [17], for ultrawideband beamforming applications. Continuous beam steering architecture and calibration method have also been proposed to partially address the resolution and phase-error issues [10], [18]. Another beamforming approach is based on the control of the phase and amplitude corresponding to each antenna element in the digital domain, which is also known as the digital beamforming architecture [9], [19]. Although a digital beamforming system has high phase and amplitude control accuracies, it usually requires a dedicated high-speed analog-to-digital converter (ADC) or a digital-to-analog converter for each antenna channel. This significantly increases the cost and power consumption of a digital beamforming system [20].

Radar systems with beam-scanning capability have been developed with techniques such as RF beamforming [10] and digital beamforming [21]. A typical beam-scanning radar system obtains the range information and azimuth angle of a target. For applications such as advanced autonomous driving, drone collision avoidance, and gesture recognition, a radar system with 2-D beam scanning provides one more dimension of information, which improves the reliability of the radar system. Conventional solutions for 2-D beam scanning include planar phased array, frequency-scanning array radar [22], [23], synthetic aperture radar (SAR) imaging [24], and multiple-input-multiple-output (MIMO) radar [25]–[27]. A planar phased array may require hundreds of antenna elements to achieve a decent 2-D angular resolution within 10°. Moreover, for the planar phased array, the requirement of a dedicated phase shifter for each antenna element makes the system complex and expensive. A frequency-scanning array radar utilizes a frequency-scanning array to provide the beam scanning capability in the third dimension. However, it has relatively poor spectrum efficiency since the frequency-scanning array requires different frequencies to steer the antenna beam. The SAR imaging approach combines a linear array and SAR imaging processing to realize 2-D scan. However, a mechanical platform or a vehicle is needed to carry the linear array. In addition, SAR imaging-based solution typically illuminates sideways. A MIMO radar system utilizes multiple transmitter and receiver channels to synthesize a larger virtual array to improve the spatial resolution. With a

Fig. 1.   Block diagram of the proposed portable K-band 3-D MIMO radar.

Fig. 2.   Four linear array distributions.

MIMO radar, it is possible to dramatically reduce the number of antenna channels while maintaining a decent 2-D angular resolution compared with the conventional 2-D beam-scanning architecture.

In this paper, a K-band MIMO frequency-modulated continuous-wave (FMCW) radar is proposed and designed. By combining the concept of MIMO and nonuniformly spaced array, high angular resolution and 2-D beam scanning can be achieved with a relatively small number of transmitter and receiver channels. A specifically designed nonuniformly spaced sparse array is used to improve the angular resolution of the radar system while removing the grating lobes in the conventional sparse array. This nonuniformly spaced array with the optimized weighting values also reduces the number of antenna channels for a specific main beamwidth and sidelobe level compared with a conventional half-wavelength spaced array. A MIMO radar prototype with eight transmitter and eight receiver channels is designed and built. With the optimized array distribution, the array and the radar transceiver are integrated on the same PCB layer. This radar prototype features a 7.2° 2-D angular resolution, a 90° field of view, a −10-dB sidelobe level, and a wireless data interface. In order to align the phases and amplitudes of each MIMO channel, a calibration procedure is also introduced. Experiments of the MIMO FMCW radar prototype reveal its capability in 3-D localization with multiple targets.

The rest of this paper is organized as follows. Section II illustrates the design principle of the proposed MIMO radar system. In Section III, the measurement results of the test structures are presented. Section IV introduces the calibration procedure of the proposed MIMO radar system. Section V demonstrates the 3-D localization experiment with the proposed MIMO radar prototype. Finally, a conclusion is drawn and future works are discussed in Section VI.

II. DESIGN PRINCIPLE

The top-level block diagram of the proposed portable K-band 3-D MIMO radar is illustrated in Fig. 1. This radar
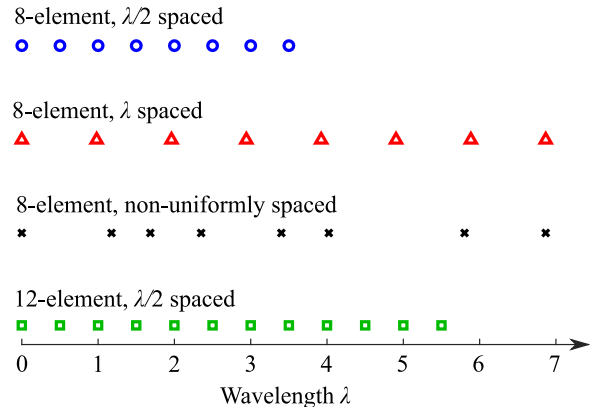
includes an RF board and a baseband module. On the RF board, a K-band phase-locked loop (PLL) is used to generate two transmitting (Tx) FMCW signal channels and one FMCW local oscillator (LO) signal channel. The two-channel Tx signals are further extended into eight channels by using customized K-band RF switches. These eight-channel signals are transmitted using an eight-element vertically distributed nonuniformly spaced linear array. On the receiver side, an eight-element horizontally distributed nonuniformly spaced linear array is used to receive the reflected FMCW signal. Two radar receiver chips are used to deramp the FMCW signal. Each of the receiver chip has four channels. After the receiver chips, eight-channel baseband signals are generated.

On the baseband part, the eight-channel baseband signals are first processed by eight channels of baseband amplifiers. Then, an eight-channel analog switch is used to select one of these eight baseband channels. The selected channel is processed by a filter and sampled by the ADC on the Wi-Fi board. The sampled baseband data are transmitted to a computer through a Wi-Fi link for further processing.

The design principles for different blocks of the proposed MIMO radar system will be discussed in detail in this section.

A. Nonuniformly Spaced Sparse Array

It is known that a sparse array can achieve a higher angular resolution with a smaller number of antenna elements. However, it suffers from the issue of grating lobes [9]. The grating lobes of the sparse array can be removed by introducing randomness in the distribution of the sparse array elements [28]–[32]. A simple comparison is illustrated in Fig. 2, where four linear arrays are shown. The first array is an eight-element linear array with $\lambda/2$ spacing between elements, where λ is the free-space wavelength. A Chebyshev window with 9.5-dB sidelobe level is applied to this array. The second linear array shown in Fig. 2 is an eight-element linear array with λ spacing between elements. The third array is a nonuniformly spaced linear array, and the last array is a 12-element $\lambda/2$-spaced linear array. The aperture sizes of the second and the third arrays are the same. The radiation patterns of these four linear arrays with their main lobes steered to −40° are illustrated in Fig. 3. The sidelobe levels of the patterns, except for the second array, are designed to be equal for a fair
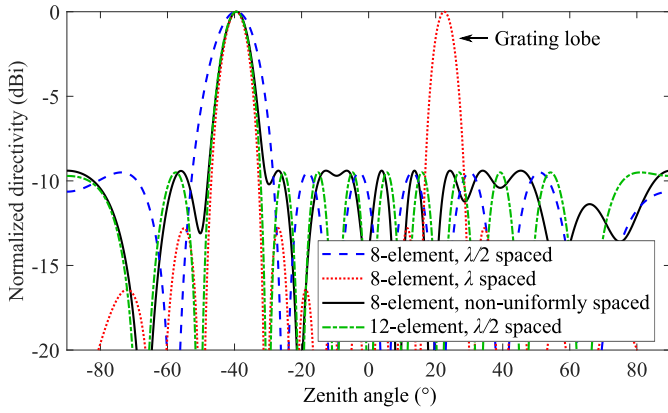
Fig. 3. Comparison among the patterns of the four linear array distributions when the main lobes are steered to $-40°$.

Fig. 4. Constraints and goal in the stochastic search method.

TABLE I
ARRAY WEIGHTING VALUES FOR FIG. 3

8-element, $\lambda/2$ spaced			
Element	**1**	**2**	**3**	**4**
Amplitude	1	0.4234	0.4746	0.5018
Phase (°)	0	−114.49	131.01	16.52
Element	**5**	**6**	**7**	**8**
Amplitude	0.5018	0.4746	0.4234	1
Phase (°)	−97.98	147.53	33.04	−81.46

8-element, λ spaced			
Element	**1**	**2**	**3**	**4**
Amplitude	1	1	1	1
Phase (°)	0	135.39	−89.23	46.16
Element	**5**	**6**	**7**	**8**
Amplitude	1	1	1	1
Phase (°)	−178.45	−43.07	92.32	−132.29

8-element, non-uniformly spaced			
Element	**1**	**2**	**3**	**4**
Amplitude	0.3645	0.9685	1	0.7889
Phase (°)	36.36	127.66	0	−131.55
Element	**5**	**6**	**7**	**8**
Amplitude	0.4371	0.8990	0.6232	0.6211
Phase (°)	−23.28	203.15	157.19	−105.06

12-element, $\lambda/2$ spaced			
Element	**1**	**2**	**3**	**4**
Amplitude	1	0.2761	0.3038	0.3258
Phase (°)	0	−114.49	131.01	16.52
Element	**5**	**6**	**7**	**8**
Amplitude	0.3411	0.3489	0.3489	0.3411
Phase (°)	−97.98	147.53	33.04	−81.46
Element	**9**	**10**	**11**	**12**
Amplitude	0.3258	0.3038	0.2761	1.0000
Phase (°)	164.05	49.55	−64.94	−179.43

comparison. The weighting values of the antenna elements to obtain the patterns shown in Fig. 3 are listed in Table I. It can be clearly observed that the first array has the broadest beamwidth when the sidelobe levels of these three arrays are all −9.5 dB. The eight-element nonuniformly spaced array can achieve similar beamwidth as the 12-element $\lambda/2$-spaced array while maintaining the advantage of a 33.3% reduction in the
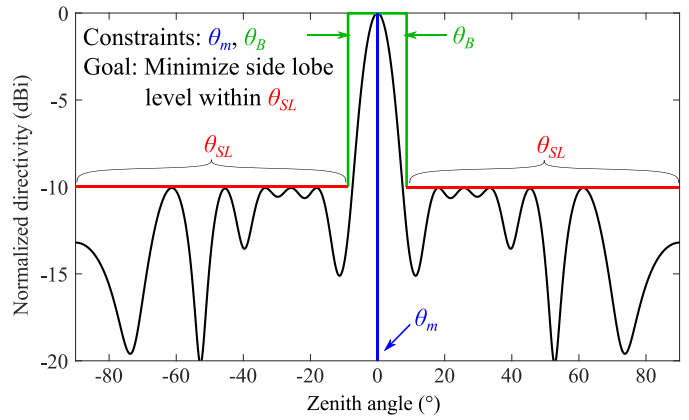
number of antenna elements. With the same aperture size, the eight-element λ-spaced array provides similar beamwidth and sidelobe level as the nonuniformly spaced array. However, the λ-spaced array has significant grating lobe issue that can be avoided by the nonuniform array.

For a conventional half-wavelength spaced array, there is a tradeoff between the main beamwidth and the sidelobe level, i.e., reducing the main beamwidth will increase the sidelobe level, and vice versa. With a sparse array, the tradeoff is not only between the main beamwidth and the sidelobe level but also with the aperture size and the element number. Typically, if the number of antenna channels is fixed, a larger aperture size leads to a narrower main beamwidth and a higher sidelobe level. On the other hand, if the aperture size and the main beamwidth are fixed, adding more antenna elements will help lower the sidelobe level. For a radar system, it is true that a radar with fewer antenna channels has a lower cost and lower power consumption. On the other hand, increasing the antenna aperture without adding more antenna channels does not significantly increase the cost. Based on this assumption, it is worthwhile to trade the aperture size for a reduced number of antenna channels and/or a reduced main beamwidth, especially for systems operating in K-band and above, where the antenna size is already small. In this paper, the design goal is to reduce both the number of antenna channels and main beamwidth.

The analytical method to obtain the optimized nonuniform distribution has yet to be developed. Researchers have been using different algorithms [28], [30]–[32] to optimize nonuniform distribution. In this paper, a stochastic search method is used to find a good nonuniform distribution for the eight-element linear array. In this method, a MATLAB program is designed to evaluate 100 000 random nonuniform distributions. The convex optimization program CVX [33] is used in the evaluations. The goal of the stochastic search method is set to find the distribution and weighting values of the array to obtain the minimal sidelobe level with the constrained main lobe location and width, as shown in Fig. 4, where θ_{SL} is the angular range of sidelobes considered. θ_m is the direction of the main lobe, and θ_B is the width constraint of the main lobe. The CVX optimization for each evaluation

TABLE II
DISTRIBUTION OF THE NONUNIFORMLY SPACED ARRAY

x_1	x_2	x_3	x_4
0	1.18λ	1.68λ	2.35λ
x_5	x_6	x_7	x_8
3.40λ	4.02λ	5.80λ	6.87λ

can be expressed as

$$w_{opt} = \arg\min_{w} \left(\max_{\theta \in \theta_{SL}} |s(\theta) \times w| \right) \quad (1)$$

$$\text{s.t. } s(\theta_m) \times w_{opt} = 1 \quad (2)$$

where

$$s(\theta) = [e^{jkx_1\sin\theta}, e^{jkx_2\sin\theta}, \dots, e^{jkx_8\sin\theta}] \quad (3)$$

where $w_{opt} = [w_1, w_2, \dots, w_8]^T$ is the optimized complex weighting value array to achieve the minimal sidelobe level with a nonuniform distribution $x = [x_1, x_2, \dots, x_8]$, as shown in Fig. 2. k is the wavenumber, T denotes the transpose operation. Equation (2) constrains the location of the main lobe to θ_m.

After 100 000 times stochastic searches, the best distribution in the 100 000 random combinations is found, which is listed in Table II. It should also be noted that this results in a good distribution but not necessarily the best one.

B. MIMO Radar

In a MIMO radar system, the virtual array concept can be applied to significantly reduce the hardware effort under the far-field conditions. It is well known that in the far-field, the radiation pattern of an array is the Fourier transform of the array distribution. Since the equivalent radiation pattern of a MIMO radar is the multiplication of the transmitter pattern and the receiver pattern, this equivalent radiation pattern can also be calculated as the Fourier transform of the convolution of the transmitter array and the receiver array. This convolution is also referred to as the virtual array [34].

Existing works in the literature [28]–[32] mainly focused on the algorithms to obtain better array distributions. They did not have a system-level design to realize a practical application. In addition, these works did not take the hardware layout for other microwave components into consideration. In this paper, the geometries of the transmitter array, the receiver array, and their corresponding virtual array of the proposed MIMO radar system are illustrated in Fig. 5. The eight-element receiver array is horizontally distributed with the geometries listed in Table II. The eight-element transmitter array is vertically distributed with the same geometries listed in Table II. With this design, the center area between the transmitter array and the receiver array is used for the integration of the radar transceiver. The equivalent virtual array is an 8×8 nonuniformly spaced planar array, as shown in Fig. 5. For convenience, each element in the virtual array is numbered as (m, n), where m denotes the row of the element and n represents the column of the element, as shown in Fig. 5.
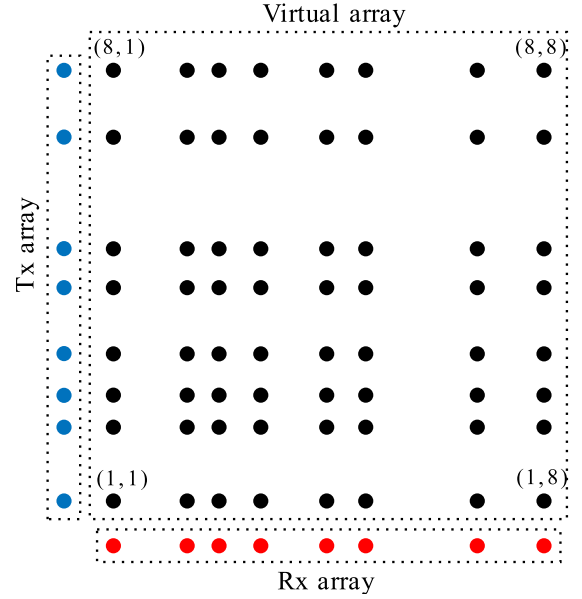

Fig. 5. Geometries of the transmitter array, receiver array, and the corresponding virtual array in the proposed MIMO radar system.
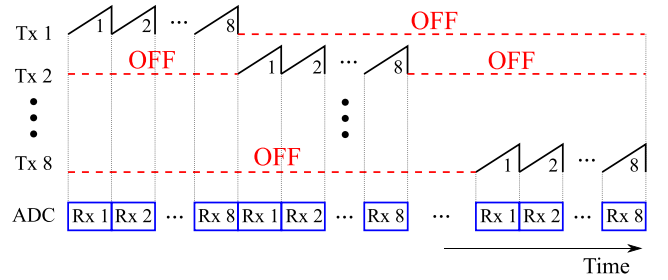

Fig. 6. Tx and Rx timing of the proposed MIMO radar system.

The receiver side of a MIMO radar needs to separate signals from different transmitters. A potential solution is using the orthogonality of orthogonal transmitter waveforms [35], [36] to identify signals from different transmitters. However, this solution requires a complex hardware design. Time-division multiplexing (TDM) is a solution that trades scanning time for simplicity. With TDM, only one transmitter works at a time, and the receivers can separate signals from different transmitters based on different time periods. Due to its simple hardware realization, TDM is used in the proposed MIMO radar. The transmitter and receiver timing of the proposed MIMO radar is illustrated in Fig. 6. Since a single-channel ADC is used in the proposed MIMO radar, only one transmitter and one receiver work at a time. 64-channel baseband data will be generated in a full scan with this radar. These 64-channel baseband data are one-to-one correspondence to the 64-virtual array elements. For example, the baseband data from Tx 4 and Rx 5 are equivalent to the baseband data from the virtual array element (4, 5).

The beamforming of the proposed MIMO radar is performed in the digital baseband. Let $s_{(m,n)}(t)$ be the time-domain signal from Tx m and Rx n, where m and n are integers from 1 to 8. $s_{(m,n)}(t)$ is also equivalent to the
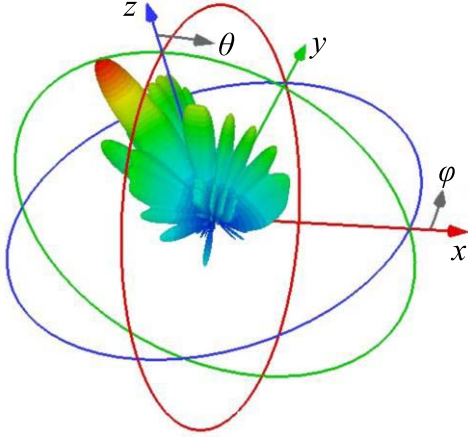
Fig. 7. Normalized 2-D radiation pattern when the beam is steered to $\theta = -20°$, $\varphi = 0°$.

time-domain signal received by virtual array element (m, n). The time-domain signal $s_{(m,n)}(t)$ can be converted to the frequency domain "range spectrum" $S_{(m,n)}(f_b)$ by Fourier transform, where the beat frequency f_b can be obtained. The range profile detected by each virtual array element $S_{(m,n)}(R)$ can be obtained with

$$R = \frac{T f_b c}{2B} \tag{4}$$

where R is the range of the target, T is the chirp repetition period of the FMCW radar, c is the speed of light, and B is the bandwidth of the chirp.

With the 64-channel range profile data, the range profile with a specific zenith angle (θ) and azimuth angle (φ) can be calculated with the digital beamforming method

$$P(\theta, \varphi, R) = w^T(\theta) \times S(R) \times w(\varphi) \tag{5}$$

where

$$S(R) = \begin{bmatrix} S_{(1,1)}(R) & S_{(1,2)}(R) & \ldots & S_{(1,8)}(R) \\ S_{(2,1)}(R) & S_{(2,2)}(R) & \ldots & S_{(2,8)}(R) \\ \vdots & \vdots & \ddots & \vdots \\ S_{(8,1)}(R) & S_{(8,2)}(R) & \ldots & S_{(8,8)}(R) \end{bmatrix} \tag{6}$$

$w(\theta)$ and $w(\varphi)$ are two lookup tables of the weighting vectors generated with the convex optimization method mentioned in Section II-A. To be more specific, $w(\theta)$ is the lookup table for the eight-element transmitter array when the main lobe is steered to the zenith angle θ; $w(\varphi)$ is the lookup table for the eight-element receiver array when the main lobe is steered to the azimuth angle φ.

An example of the 2-D beamforming pattern with the proposed MIMO radar is illustrated in Fig. 7, where the main lobe is steered to $\theta = -20°$ and $\varphi = 0°$. This 2-D pattern is simulated with the CST Microwave Studio. The array elements are circular microstrip patches. The beamwidth of the main lobe is 7.2° and the sidelobe is about -9.5 dB.

C. Patch Antenna

Circular patch antennas are used as the radiation element in the proposed MIMO radar. The layout of the circular
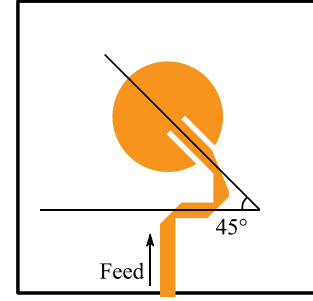

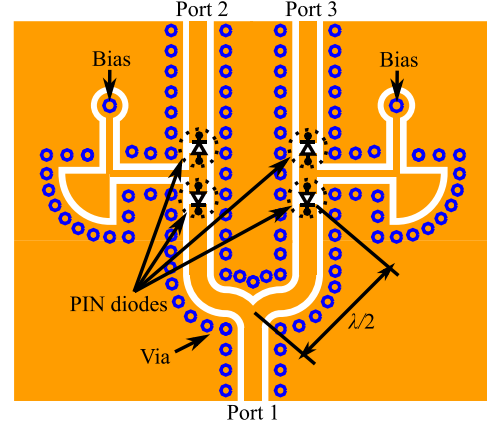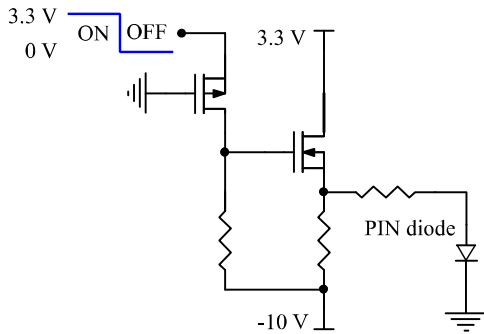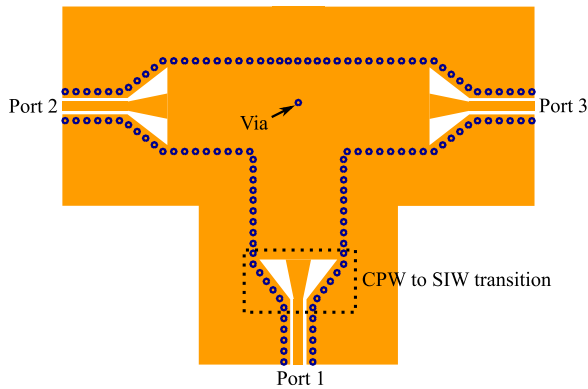Fig. 8. Layout of the circular patch antenna.

Fig. 9. Layout of the customized K-band SPDT switch.

patch antenna is illustrated in Fig. 8. The diameter of the patch is about 4 mm. In order to align the polarization for the transmitter and the receiver elements, the circular patch antenna is tilted by 45°.

D. K-Band SPDT Switch

To extend the number of transmitter channels, a K-band single-pole-double-throw (SPDT) switch is designed based on a microwave structure and p-i-n diodes. The layout of the K-band SPDT switch is shown in Fig. 9. There are three ports on this K-band SPDT switch. Port 1 is the input port. Ports 2 and 3 are the output ports. Two p-i-n diodes are placed on each path connected to port 2 or port 3 to improve the isolation in the OFF state. The distance from the p-i-n diodes to the junction is about half-wavelength. If the p-i-n diodes are forward biased, the corresponding path is turned ON. Otherwise, the path is turned OFF.

The schematic of the bias circuit used to control the K-band SPDT switch is shown in Fig. 10. This bias circuit has a pMOS transistor, an nMOS transistor, and several resistors. The basic function of the bias circuit is to convert the common digital binary voltages 0 and 3.3 V to the special binary biases for the p-i-n diodes. The values of the resistors are optimized to reverse bias the p-i-n diode with -10 V to turn OFF the RF path when the input of the bias circuit is 0 V. On the other hand, the optimized resistor values also make sure the p-i-n diode is forward biased with 30-mA current to turn ON the RF path with the input of 3.3 V.

Fig. 10. Bias circuit for the K-band SPDT switch.

Fig. 11. Layout of the K-band SIW power divider.

E. K-Band SIW Power Divider

A K-band power divider is designed to distribute the LO signal to two receiver chips. This power divider is built with the coplanar waveguide (CPW) and substrate integrated waveguide (SIW). The layout of the K-band power divider is illustrated in Fig. 11. A CPW to SIW transition structure is used to convert the CPW to SIW. This K-band SIW power divider features simple structure and is easy to fabricate in the standard printed circuit board fabrication process.

III. TEST STRUCTURES

Separate discrete structures used in the proposed MIMO radar have been fabricated for characterization purpose. Rogers RO3003 with 0.245 mm thickness is chosen as the substrate of these structures. The dielectric constant is 3 and its loss tangent is 0.001.

A. Patch Antenna

A photograph of the fabricated circular patch antenna is shown in Fig. 12. Fig. 13 illustrates the simulated radiation patterns of the designed circular patch antenna, where Fig. 13(a) is the E-plane pattern and Fig. 13(b) is the H-plane pattern. The beamwidths on both the E- and the H-planes are about 90°. Fig. 14 shows the simulated and measured S_{11} of the designed circular patch antenna. The center frequency in the simulation is 24.125 GHz. However, due to fabrication errors, the measured S_{11} of the fabricated circular patch antenna
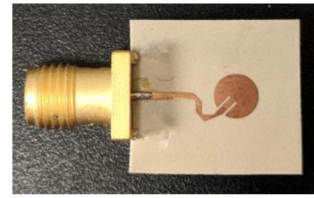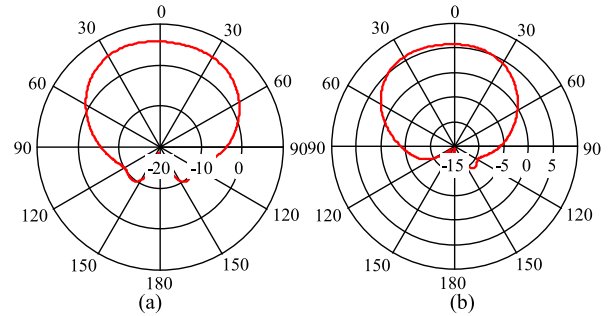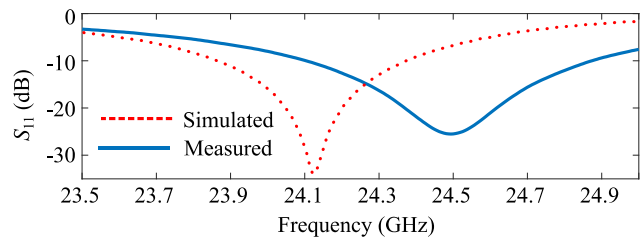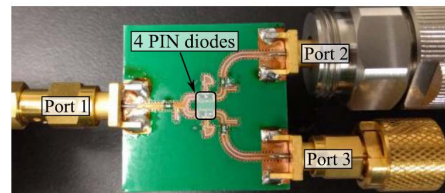

Fig. 12. Photograph of the fabricated circular patch antenna.

Fig. 13. Simulated radiation patterns of the circular patch antenna. (a) E-plane. (b) H-plane.

Fig. 14. Simulated and measured S_{11} of the circular patch antenna.

Fig. 15. Photograph of the fabricated K-band SPDT switch.

shifted to 24.5 GHz. Since the measured S_{11} at 24.125 GHz is around −9 dB, this antenna can still work at 24.125 GHz with a slight degradation of the performance.

B. K-Band SPDT Switch

The photograph of the test structure for the K-band SPDT switch is illustrated in Fig. 15. The measured S_{21} at 24.125 GHz in the ON state is around −1.2 dB, which is about 0.2 dB lower than the simulated result after deembedding the loss introduced by the SMA connectors, as shown in Fig. 16. When the path is turned OFF, the simulated S_{21} is about −24 dB and the measured S_{21} is about −18 dB. The isolation between ports 2 and 3 is better than 26 dB. The simulated and measured S_{11} and S_{22} of the fabricated K-band SPDT switch are shown in Fig. 17, both the simulated and measured results
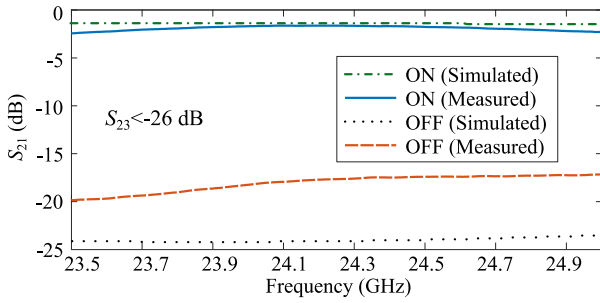
Fig. 16. Simulated and measured S_{21} of the K-band SPDT switch in the ON and OFF states.
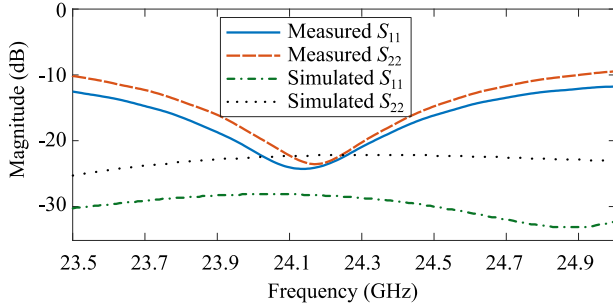

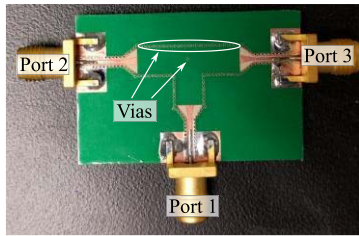Fig. 17. Simulated and measured S_{11} and S_{22} of the fabricated K-band SPDT switch.

Fig. 18. Photograph of the fabricated K-band SIW power divider.
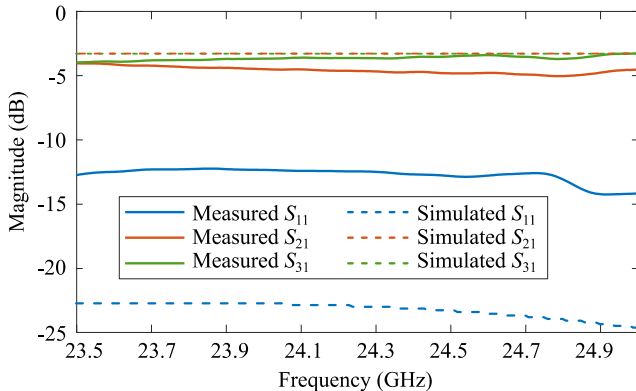

Fig. 19. Simulated and measured S-parameters of the fabricated K-band SIW power divider.

are below -20 dB at 24.125 GHz. The simulated performance is better due to the use of a relatively ideal p-i-n diode model.

C. K-Band SIW Power Divider

The photograph of the fabricated K-band SIW power divider is shown in Fig. 18. Fig. 19 depicts the simulated and measured S-parameters of the power divider. The simulation
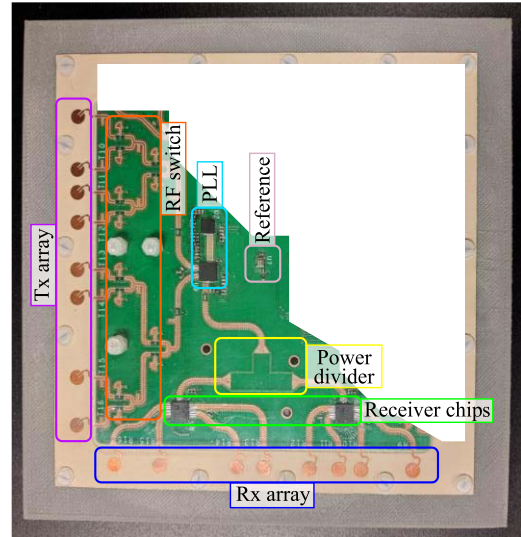

Fig. 20. Photograph of the RF board of the K-band 3-D MIMO radar prototype.

based on a relatively ideal model shows -3-dB insertion losses in S_{21} and S_{31}. The measured insertion losses from port 1 to ports 2 and 3 are -3.2 and -4.2 dB at 24.125 GHz after deembedding the loss of the SMA connectors, respectively. S_{11} of port 1 is below -13 dB.

IV. RADAR PROTOTYPE AND CALIBRATION

A K-band 3-D MIMO radar prototype has been built. This radar prototype consists of an RF board, a baseband board, and a Wi-Fi board. The photograph of the RF board is shown in Fig. 20. Both the width and height of the RF board are 120 mm. The substrate of the RF board is Rogers RO3003 with 0.254 mm thickness. The locations of the major components are also shown in Fig. 20. Fig. 21(a) is the photograph of the baseband board, which includes a power supply, a -10-V dc–dc converter, an eight-channel baseband amplifier, and bias circuits for the SPDT switches. On the backside of the baseband board, a customized Wi-Fi board is stacked, as shown in Fig. 21(b). The substrate of the baseband board and the Wi-Fi board is FR4. The photograph of the fully assembled radar prototype is shown in Fig. 22. The RF board and the baseband board are connected by flat cables and ribbon wires. The flat cables are used for power supply, digital control, and baseband signal routing. The ribbon wires are used for biasing the SPDT switches.

The major components of the K-band 3-D MIMO radar prototype are listed in Table III. The 24-GHz radar transceiver chipset from analog devices, including ADF4159, ADF5901, and ADF5904, are used in the prototype. The p-i-n diodes used in the K-band SPDT switches are MADP-000907-14020W from MACOM. On the Wi-Fi board, Texas Instruments Incorporated's CC3200 Wi-Fi chip, which combines an ARM Cortex-M4 and a Wi-Fi subsystem, is used to sample the baseband signal and send the data to a computer through Wi-Fi. CC3200 is also used as the controller to configure the transceiver chipset.
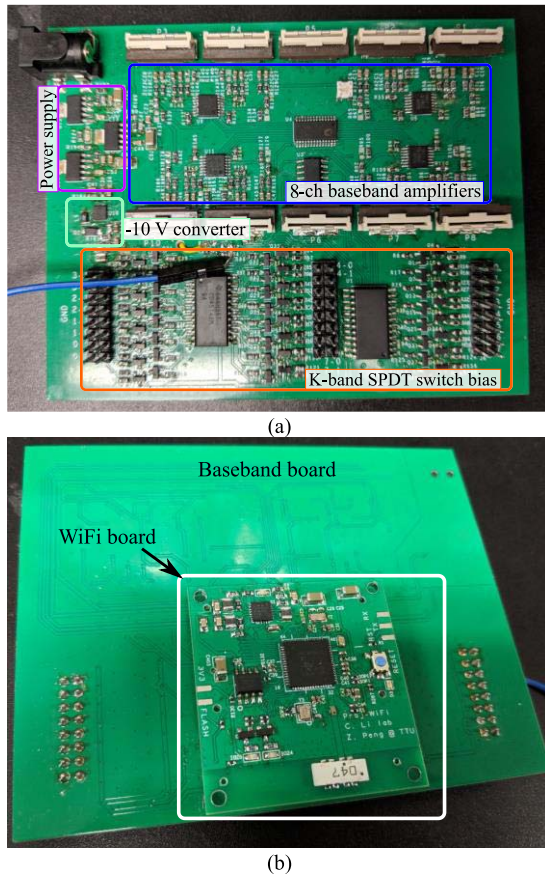
(a)

(b)

Fig. 21. Photograph of the baseband part of the K-band 3-D MIMO radar prototype. (a) Baseband board. (b) Wi-Fi board.
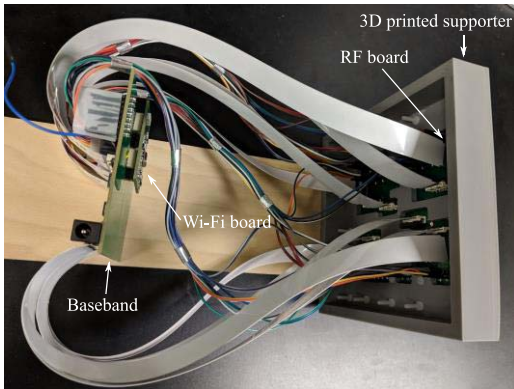

Fig. 22. Photograph of the fully assembled radar prototype.

TABLE III

MAIN COMPONENTS USED IN THE MIMO RADAR PROTOTYPE

Part	Device	Manufacturer	Function
RF board	520L15IA40M0000	CTS	Clock
	ADF4159	Analog Devices	PLL
	ADF5901	Analog Devices	VCO
	ADF5904	Analog Devices	Receiver
	MADP-000907-14020W	MACOM	PIN diode
Baseband board	TPS7A4501DCQR	Texas Instruments	Regulator
	TPS63700	Texas Instruments	DC-DC converter
	CD74AC138	Texas Instruments	Decoder
	CD4514B	Texas Instruments	Decoder
	ADA4851	Analog Devices	OpAmp
	ADG706	Analog Devices	Analog switch
Wi-Fi board	CC3200	Texas Instruments	Wi-Fi and ARM
	DEA162450BT	Filter	TDK
	AH104F	Antenna	Yuden
	ADP5135	Analog Devices	dc-dc
	AT25SF161	Adesto	Flash

TABLE IV

BASIC PARAMETERS OF THE MIMO RADAR PROTOTYPE

Tx power	0 dBm	Center frequency	24.125 GHz
Tx bandwidth	240 MHz	Sampling rate	250 ksps
Chirp repetition period	10 ms	Power consumption	2.5 W

the Wi-Fi board on the radar prototype will create a Wi-Fi access point, which can be connected by a computer or a portable device through a Wi-Fi adaptor. After connected, the designed program can be used to send commands to the radar prototype through the transmission control protocol (TCP) sockets. The sampled baseband data are recorded by the program using the user datagram protocol (UDP) sockets. The TCP sockets guarantee a reliable radar system control, and the UDP sockets are used to achieve the maximum data transmission rate. MATLAB is used for the postprocessing of the recorded baseband data.

Calibration is one of the most important parts of the proposed K-band 3-D MIMO radar. Since the signal paths of different transmitter and receiver channels have different lengths and losses/gains in the built MIMO radar prototype, a calibration is required to compensate for these variations.

The electrical parameters of the radar prototype are listed in Table IV. The transmitting power of each transmitter is about 0 dBm with a center frequency of 24.125 GHz. The bandwidth of the chirp signal is 240 MHz, and the chirp repetition period is 10 ms. By combing the four ADC channels in CC3200, the maximum sampling rate can reach 250 ksps. This radar is powered by 5-V dc voltage, and its average power consumption is about 2.5 W.

A program was also built to communicate with the radar prototype. This program was programmed with QT, a C++ cross-platform SDK. When the radar prototype is powered ON,

Fig. 23. Photograph of the calibration setup.

Fig. 24. Uncalibrated range profiles of the 64-channel beat signals. (a) Amplitudes in Calibration A. (b) Phases in Calibration A. (c) Amplitudes in Calibration B. (d) Phases in Calibration B.
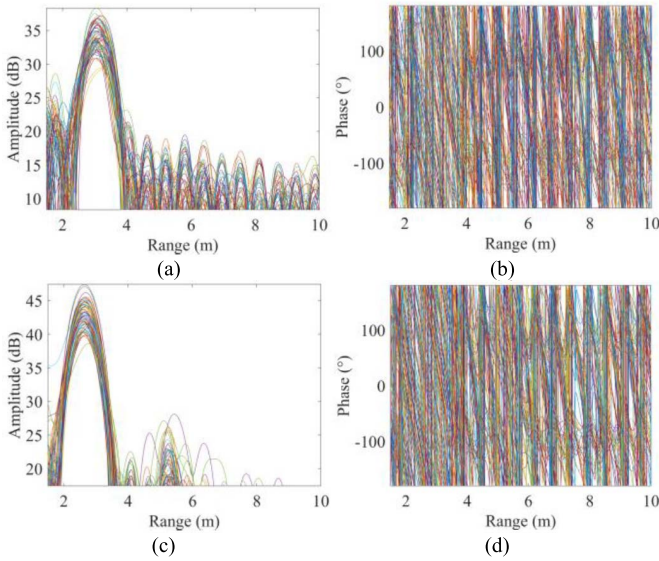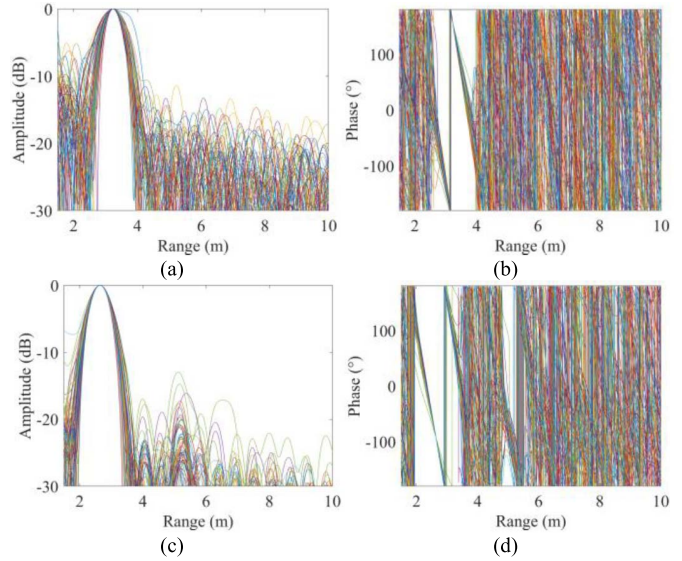

Fig. 25. Calibrated range profiles of the 64-channel beat signals. (a) Amplitudes in Calibration A. (b) Phases in Calibration A. (c) Amplitudes in Calibration B. (d) Phased in Calibration B.
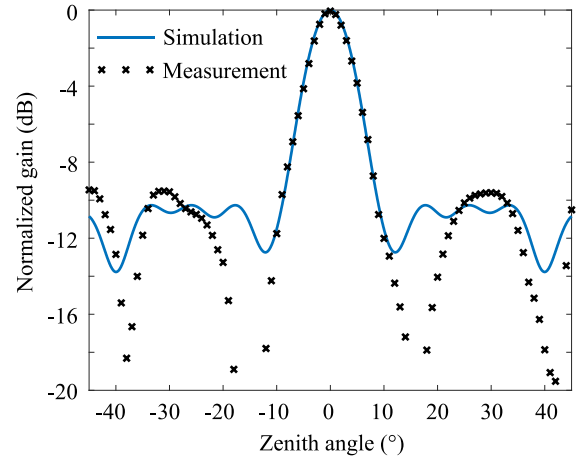

Fig. 26. Measured horizontal pattern in the field of view when the beam is steered to 0°.

The calibration was performed in an open field with a corner reflector placed in front of the MIMO radar prototype, as shown in Fig. 23. The radar prototype was put on the back of a car, and it was powered by the cigarette lighter of the car with a 12-to-5-V converter. The centers of the corner reflector and the radar prototype were aligned. The basic idea of the calibration is based on the concept that the signals received by all the antennas have the same phase and amplitude for an ideal radar system in far-field condition when a single target is in front of the radar with their centers aligned. Thus, with the calibration setup in Fig. 23, the amplitude and phase differences among antennas are introduced by the RF path delays and component variations. By correcting these phase and amplitude differences in the digital signal processing stage, the radar prototype is calibrated.

Two calibrations, Calibration A and Calibration B, have been performed. During Calibration A, the distance between the radar prototype and the corner reflector was 3.2 m. In Calibration B, the distance was 2.6 m. Fig. 24 shows the uncalibrated range profiles of the 64-channel beat signals. Fig. 24(a) and (b) is the amplitudes and phases of

Calibration A. Fig. 24(c) and (d) is the amplitudes and phases of Calibration B. Using the first channel in each calibration as the reference, the calibration procedure normalizes the amplitudes and aligns the ranges and phases of each range profile to the references at the location of the corner reflector. The calibrated amplitudes and phases are plotted in Fig. 25. Fig. 25(a) and (b) is the calibrated amplitudes and phases of Calibration A. Fig. 25(c) and (d) is the calibrated amplitudes and phases of Calibration B. It can be observed that Calibration B has a better signal-to-noise ratio (SNR) at the target location than that of Calibration A. The offsets of ranges, amplitudes, and phases are recorded to form calibration matrices. The matrices will be applied to the signal processing of the measurement data.

The comparison of the main beamwidth and the sidelobe level between the simulation and the measurement after the calibration is illustrated in Fig. 26. The measured main beamwidth matches well with the simulated result. The measured sidelobe level is 1 dB higher than the simulated sidelobe level, which is acceptable.
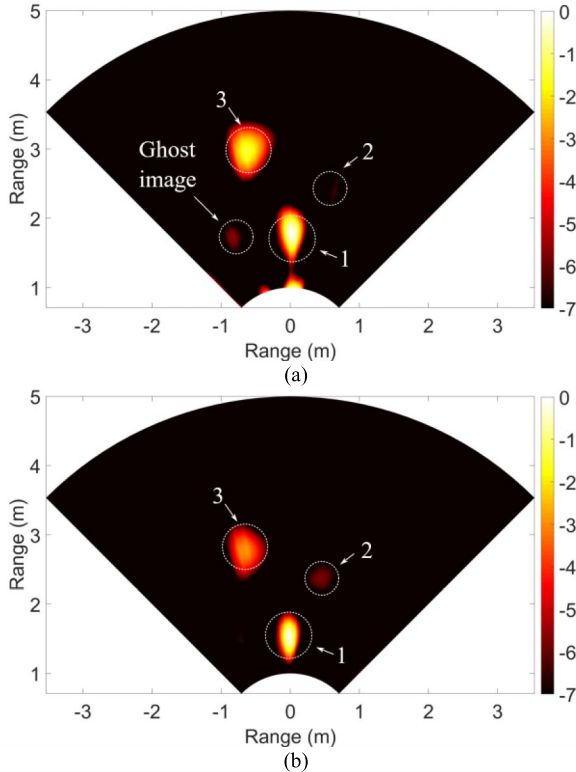
Fig. 27.　Photograph of the experimental setup.

(a)

(b)

Fig. 28.　2-D localization with Tx 1 and Rx 1-8. (a) With Calibration A. (b) With Calibration B.

V. EXPERIMENT AND DISCUSSION

An experiment of 3-D localization has been performed with the built K-band 3-D MIMO radar prototype. The experimental setup is shown in Fig. 27. In this experiment, the radar prototype was put on the back of a car, and three corner reflectors, which have different heights, were placed in front of the radar prototype at different locations. 64-channel beat signals can be obtained in one full scan with the radar prototype. The time for a full scan is 0.64 s. Using the data transmitted by Tx 1 and received by Rx 1-8, which are the signals of virtual elements $(1, 1), (1, 2), \ldots, (1, 8)$, a 2-D localization map of the targets on the horizontal plane can be obtained. Fig. 28 plots the 2-D localization maps of the targets on the horizontal plane with the two calibration

TABLE V
COMPARISON AMONG THE EXISTING SOLUTIONS AND THE PROPOSED WORK IN THIS PAPER

	Phased array radar	Conventional MIMO radar	This work
Array geometries		($\blacksquare$: Rx, $\square$: Tx)	Fig. 5
Element number	1 Tx + 12 × 12 Rx	12 Tx + 12 Rx	8 Tx + 8 Rx
Scanning time	12 × 12T	[a]12 × 12T [b]12T	[a]8 × 8T [c]8T

a: With a single-channel ADC.
b: With a 12-channel ADC.
c: With an eight-channel ADC.

matrices obtained in Section IV. Fig. 28(a) is the result of applying the calibration matrices obtained in Calibration A, and Fig. 28(b) is the same measurement with the calibration matrices obtained in Calibration B. In Fig. 28(a), the signature of target 2 is very weak, and a ghost signature can be observed. On the other hand, in Fig. 28(b), the signatures of the three targets are clear, and no ghost signature is observed. The results in Fig. 28 reveal that the calibration matrices obtained in Calibration B provide a better imaging result since it has the better SNR than that of Calibration A.

3-D localization can be obtained with all the 64-channel data measured by the MIMO radar prototype. Fig. 29 shows the images of the 3-D localization of three corner reflectors based on the calibration matrices obtained in Calibration B. It can be clearly seen that the three corner reflectors are located at 1.6, 2.3, and 3.14 m with different azimuth and zenith angles. The estimated range accuracy of the system is about 5 cm and the angular accuracy is about 3° using the measurement results from a tape meter as the reference.

It is worth noting that the implemented TDM scheme still has a room to improve, such as using multichannel ADCs, increasing the chirp repetition frequency, and reducing the chirp length. However, these improvements are mainly engineering optimization for the baseband parts. The concept and architecture of the array and radar transceiver will not be changed. The proposed radar front end with a powerful baseband could be a good solution for applications of indoor human tracking, security surveillance, robot/drone navigation, and autonomous vehicles.

A comparison among the phased array radar, conventional MIMO radar, and the proposed radar in this paper is listed in Table V. This comparison is based on the realization of a radar system with 2-D beam-scanning capability. The field of view of the design is 90° and the 2-D angular resolution is 7.2°. The sidelobe level of the antenna beam is −9.5 dB. As shown in Table V, it requires a 12 × 12 planar array to achieve the design goals, and each array element needs a dedicated phase shifter. For a conventional MIMO radar, 12 transmitters and 12 receivers are necessary. However, with the design
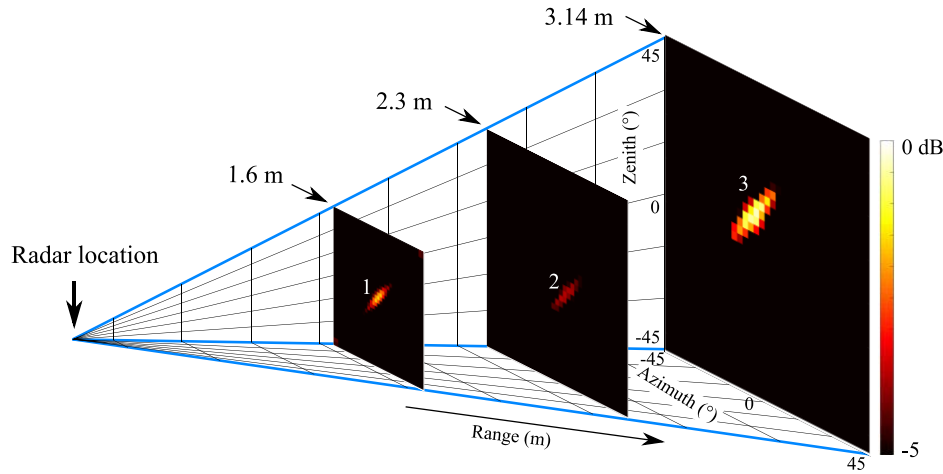
Fig. 29.   3-D images of the three targets with the MIMO radar prototype.

proposed in this paper, it only needs eight transmitters and eight receivers to achieve the 2-D beam-scanning design goals. Regarding the scanning time, the phased array approach scans the field of view by steering the beam angle by angle. It requires about $12 \times 12 \ T$ to finish a scan, where T is the chirp repetition period for the FMCW radar. On the other hand, the conventional TDM-based MIMO radar also needs $12 \times 12 \ T$ to finish a scan with a single-channel ADC. Its scanning time can be reduced to $12 \ T$ by using a 12-channel ADC to sample the 12-channel receivers in parallel. With the proposed MIMO radar system, the scanning time is $8 \times 8 \ T$ with a single-channel ADC. It can be reduced to $8 \ T$ by using an eight-channel ADC to sample the receivers in parallel.

VI. Conclusion

In this paper, a K-band portable 3-D MIMO FMCW radar system with nonuniformly spaced array has been designed and built. By combining the concept of MIMO and nonuniformly spaced array, higher angular resolution and 2-D beam-scanning capabilities can be achieved with a relatively smaller number of transmitter and receiver channels in the designed K-band MIMO FMCW radar. A specifically designed nonuniformly spaced sparse array is used to improve the angular resolution of the radar system, as well as removing the grating lobes in a conventional sparse array. The built MIMO radar prototype with eight transmitter channels and eight receiver channels features $7.2°$ 2-D angular resolution, $90°$ field of view, -9.5-dB sidelobe level, and wireless data transfer. In order to align the phases and amplitudes of each MIMO channel, a calibration procedure was introduced. Experiments of the MIMO FMCW radar prototype revealed its capability in 3-D localization with multiple targets. Potential applications of the proposed MIMO radar system can be short-range localization, robot/drone navigation, and autonomous vehicles.

References

[1] F. Ahmad and M. G. Amin, "Noncoherent approach to through-the-wall radar localization," *IEEE Trans. Aerosp. Electron. Syst.*, vol. 42, no. 4, pp. 1405–1419, Oct. 2006.

[2] E. J. Baranoski, "Through wall imaging: Historical perspective and future directions," in *Proc. IEEE Int. Conf. Acoust., Speech Signal Process. (ICASSP)*, Mar./Apr. 2008, pp. 5173–5176.

[3] M. Vossiek, L. Wiebking, P. Gulden, J. Wieghardt, C. Hoffmann, and P. Heide, "Wireless local positioning," *IEEE Microw. Mag.*, vol. 4, no. 4, pp. 77–86, Dec. 2003.

[4] D. M. Grimes and T. O. Jones, "Automotive radar: A brief review," *Proc. IEEE*, vol. 62, no. 6, pp. 804–822, Jun. 1974.

[5] J. Hatch, A. Topak, R. Schnabel, T. Zwick, R. Weigel, and C. Waldschmidt, "Millimeter-wave technology for automotive radar sensors in the 77 GHz frequency band," *IEEE Trans. Microw. Theory Techn.*, vol. 60, no. 3, pp. 845–860, Mar. 2012.

[6] C. Li, V. M. Lubecke, O. Boric-Lubecke, and J. Lin, "A review on recent advances in Doppler radar sensors for noncontact healthcare monitoring," *IEEE Trans. Microw. Theory Techn.*, vol. 61, no. 5, pp. 2046–2060, May 2013.

[7] R. Rotman, "Recent advances using microwaves for imaging, hyperthermia and interstitial ablation of breast cancer tumors," in *Proc. IEEE Int. Conf. Microw., Commun., Antennas Electron. Syst. (COMCAS)*, Nov. 2011, pp. 1–4.

[8] B. Schleicher, I. Nasr, A. Trasser, and H. Schumacher, "IR-UWB radar demonstrator for ultra-fine movement detection and vital-sign monitoring," *IEEE Trans. Microw. Theory Techn.*, vol. 61, no. 5, pp. 2076–2085, May 2013.

[9] H. J. Visser, *Array and Phased Array Antenna Basics*. Hoboken, NJ, USA: Wiley, 2006.

[10] Z. Peng, L. Ran, and C. Li, "A K-band portable FMCW radar with beamforming array for short-range localization and vital-Doppler targets discrimination," *IEEE Trans. Microw. Theory Techn.*, vol. 65, no. 9, pp. 3443–3452, Sep. 2017.

[11] W.-T. Li, Y.-C. Chiang, J.-H. Tsai, H.-Y. Yang, J.-H. Cheng, and T.-W. Huang, "60-GHz 5-bit phase shifter with integrated VGA phase-error compensation," *IEEE Trans. Microw. Theory Techn.*, vol. 61, no. 3, pp. 1224–1235, Mar. 2013.

[12] A. Asoodeh and M. Atarodi, "A full 360° vector-sum phase shifter with very low RMS phase error over a wide bandwidth," *IEEE Trans. Microw. Theory Techn.*, vol. 60, no. 6, pp. 1626–1634, Jun. 2012.

[13] M. Longbrake, "True time-delay beamsteering for radar," in *Proc. IEEE Nat. Aerosp. Electron. Conf. (NAECON)*, Jul. 2013, pp. 246–249.

[14] M. Kim, J. B. Hacker, R. E. Mihailovich, and J. F. DeNatale, "A DC-to-40 GHz four-bit RF MEMS true-time delay network," *IEEE Microw. Wireless Compon. Lett.*, vol. 11, no. 2, pp. 56–58, Feb. 2001.

[15] N. S. Barker and G. M. Rebeiz, "Distributed MEMS true-time delay phase shifters and wide-band switches," *IEEE Trans. Microw. Theory Techn.*, vol. 46, no. 11, pp. 1881–1890, Nov. 1998.

[16] X. Tang and K. Mouthaan, "Large bandwidth digital phase shifters with all-pass, high-pass, and low-pass networks," *IEEE Trans. Microw. Theory Techn.*, vol. 61, no. 6, pp. 2325–2331, Jun. 2013.

[17] X. Tang and K. Mouthaan, "Design of large bandwidth phase shifters using common mode all-pass networks," *IEEE Microw. Wireless Compon. Lett.*, vol. 22, no. 2, pp. 55–57, Feb. 2012.

[18] Z. Peng *et al.*, "Radio frequency beamforming based on a complex domain frontend," *IEEE Trans. Microw. Theory Techn.*, vol. 64, no. 1, pp. 289–298, Jan. 2016.

[19] R. Miura, T. Tanaka, I. Chiba, A. Horie, and Y. Karasawa, "Beamforming experiment with a DBF multibeam antenna in a mobile satellite environment," *IEEE Trans. Antennas Propag.*, vol. 45, no. 4, pp. 707–714, Apr. 1997.

[20] A. Matsuzawa, "Trends in high speed ADC design," in *Proc. 7th Int. Conf. (ASIC)*, 2007, pp. 245–248.

[21] R. Feger, C. Wagner, S. Schuster, S. Scheiblhofer, H. Jager, and A. Stelzer, "A 77-GHz FMCW MIMO radar based on an SiGe single-chip transceiver," *IEEE Trans. Microw. Theory Techn.*, vol. 57, no. 5, pp. 1020–1035, May 2009.

[22] T. Geibig, A. Shoykhetbrod, A. Hommes, R. Herschel, and N. Pohl, "Compact 3D imaging radar based on FMCW driven frequency-scanning antennas," in *Proc. IEEE Radar Conf. (RadarConf)*, May 2016, pp. 1–5.

[23] A. Shoykhetbrod, T. Geibig, A. Hommes, R. Herschel, and N. Pohl, "Concept for a fast tracking 60 GHz 3D-radar using frequency scanning antennas," in *Proc. 41st Int. Conf. Infr., Millim., Terahertz Waves (IRMMW-THz)*, Sep. 2016, pp. 1–3.

[24] X. Zhuge and A. G. Yarovoy, "A sparse aperture MIMO-SAR-based UWB imaging system for concealed weapon detection," *IEEE Trans. Geosci. Remote Sens.*, vol. 49, no. 1, pp. 509–518, Jan. 2011.

[25] M. Harter, A. Ziroff, and T. Zwick, "Three-dimensional radar imaging by digital beamforming," in *Proc. Eur. Radar Conf. (EuRAD)*, 2011, pp. 17–20.

[26] D. Bleh *et al.*, "*W*-band time-domain multiplexing FMCW MIMO radar for far-field 3-D imaging," *IEEE Trans. Microw. Theory Techn.*, vol. 65, no. 9, pp. 3474–3484, Sep. 2017.

[27] S. S. Ahmed, A. Schiessl, and L.-P. Schmidt, "A novel fully electronic active real-time imager based on a planar multistatic sparse array," *IEEE Trans. Microw. Theory Techn.*, vol. 59, no. 12, pp. 3567–3576, Dec. 2011.

[28] R. L. Haupt, "Thinned arrays using genetic algorithms," *IEEE Trans. Antennas Propag.*, vol. 42, no. 7, pp. 993–999, Jul. 1994.

[29] M. Andreasen, "Linear arrays with variable interelement spacings," *IRE Trans. Antennas Propag.*, vol. 10, no. 2, pp. 363–369, Mar. 1962.

[30] K. Chen, Z. He, and C. C. Han, "A modified real GA for the sparse linear array synthesis with multiple constraints," *IEEE Trans. Antennas Propag.*, vol. 54, no. 7, pp. 2169–2173, Jul. 2006.

[31] R. Bhattacharya, T. K. Bhattacharyya, and R. Garg, "Position mutated hierarchical particle swarm optimization and its application in synthesis of unequally spaced antenna arrays," *IEEE Trans. Antennas Propag.*, vol. 60, no. 7, pp. 3174–3181, Jul. 2012.

[32] T. Pavlenko, C. Reustle, Y. Dobrev, M. Gottinger, L. Jassoume, and M. Vossiek, "Design and optimization of sparse planar antenna arrays for wireless 3-D local positioning systems," *IEEE Trans. Antennas Propag.*, vol. 65, no. 12, pp. 7288–7297, Dec. 2017.

[33] M. Grant and S. Boyd. (Mar. 2014). *CVX: MATLAB Software for Disciplined Convex Programming, Version 2.1*. [Online]. Available: http://cvxr.com/cvx

[34] F. C. Robey, S. Coutts, D. Weikle, J. C. McHarg, and K. Cuomo, "MIMO radar theory and experimental results," in *Proc. Conf. Rec. 38th Asilomar Conf. Signals, Syst. Comput.*, vol. 1, 2004, pp. 300–304.

[35] J. L. J. Liang and Q. L. Q. Liang, "Orthogonal waveform design and performance analysis in radar sensor networks," in *Proc. IEEE Mil. Commun. Conf. (MILCOM)*, Oct. 2006, pp. 1–6.

[36] X. Wu, Z. Tian, T. N. Davidson, and G. B. Giannakis, "Optimal waveform design for UWB radios," *IEEE Trans. Signal Process.*, vol. 54, no. 6, pp. 2009–2021, Jun. 2006.

Zhengyu Peng (S'15) received the B.S. and M.Sc. degrees in electrical engineering from Zhejiang University, Hangzhou, China, in 2011 and 2014, respectively, and the Ph.D. degree in electrical engineering from Texas Tech University, Lubbock, TX, USA, in 2018.

In 2017, he was with the Mitsubishi Electric Research Laboratories, Cambridge, MA, USA, where he was involved in the novel design of digital beamforming transmitter architecture for radars and MIMO systems. He is currently a Senior Radar Systems Engineer with Aptiv, Kokomo, IN, USA. His current research interests include automotive radar, antennas, microwave circuits, and biomedical applications of microwave/RF circuits and systems.

Dr. Peng was a recipient of the 2016 IEEE Microwave Theory and Techniques Society Graduate Fellowship, the Excellent Demo Track Presentation Award of the 2016 IEEE Radio and Wireless Week, and the Third Place of the Student Design Competition for high sensitivity radar of the 2015 IEEE MTT-S International Microwave Symposium. He was a Reviewer for more than 50 journal papers, including the IEEE TRANSACTIONS ON MICROWAVE THEORY AND TECHNIQUES, the IEEE TRANSACTIONS ON INSTRUMENTATION AND MEASUREMENT, the IEEE TRANSACTIONS ON CIRCUITS AND SYSTEMS—I: REGULAR PAPERS, the IEEE TRANSACTIONS ON CIRCUITS AND SYSTEMS—II: EXPRESS BRIEFS, the IEEE TRANSACTIONS ON MOBILE COMPUTING, and the IEEE TRANSACTIONS ON BIOMEDICAL ENGINEERING.

Changzhi Li (S'06–M'09–SM'13) received the B.S. degree in electrical engineering from Zhejiang University, Hangzhou, China, in 2004, and the Ph.D. degree in electrical engineering from the University of Florida, Gainesville, FL, USA, in 2009.

From 2007 to 2009, he was with Alereon Inc., Austin, TX, USA, and Coherent Logix Inc., Austin, where he was involved in ultra-wideband transceivers and software-defined radio. He joined Texas Tech University, Lubbock, TX, USA, as an Assistant Professor in 2009, and became an Associate Professor in 2014. His current research interests include biomedical applications of microwave/RF, wireless sensor, and analog circuits.

Dr. Li served as the TPC Co-Chair for the IEEE MTT-S International Microwave Biomedical Conference in 2018 and the IEEE Wireless and Microwave Technology Conference in 2012 and 2013. He was a recipient of the IEEE Microwave Theory and Techniques Society (MTT-S) Outstanding Young Engineer Award in 2018, the ASEE Frederick Emmons Terman Award in 2014, the IEEE-HKN Outstanding Young Professional Award in 2014, the NSF Faculty Early CAREER Award in 2013, the IEEE MTT-S Graduate Fellowship Award in 2008, and a few Best Paper Awards as author/advisor in IEEE-sponsored conferences. He was an Associate Editor of the IEEE TRANSACTIONS ON CIRCUITS AND SYSTEMS—II: EXPRESS BRIEFS in 2014 and 2015. He is currently an Associate Editor of the IEEE TRANSACTIONS ON CIRCUITS AND SYSTEMS—I: REGULAR PAPERS.